

# An Optimal Radial Profile Order Based on the Golden Ratio for Time-Resolved MRI

Stefanie Winkelmann\*, Tobias Schaeffter, Thomas Koehler, Holger Eggers, and Olaf Doessel

**Abstract**—In dynamic magnetic resonance imaging (MRI) studies, the motion kinetics or the contrast variability are often hard to predict, hampering an appropriate choice of the image update rate or the temporal resolution. A constant azimuthal profile spacing ( $111.246^\circ$ ), based on the Golden Ratio, is investigated as optimal for image reconstruction from an arbitrary number of profiles in radial MRI. The profile order is evaluated and compared with a uniform profile distribution in terms of signal-to-noise ratio (SNR) and artifact level. The favorable characteristics of such a profile order are exemplified in two applications on healthy volunteers. First, an advanced sliding window reconstruction scheme is applied to dynamic cardiac imaging, with a reconstruction window that can be flexibly adjusted according to the extent of cardiac motion that is acceptable. Second, a contrast-enhancing  $k$ -space filter is presented that permits reconstructing an arbitrary number of images at arbitrary time points from one raw data set. The filter was utilized to depict the T1-relaxation in the brain after a single inversion prepulse. While a uniform profile distribution with a constant angle increment is optimal for a fixed and predetermined number of profiles, a profile distribution based on the Golden Ratio proved to be an appropriate solution for an arbitrary number of profiles.

**Index Terms**—Projection reconstruction, radial signal-to-noise ratio (MRI), real-time imaging, time-resolved imaging.

## I. INTRODUCTION

IN RADIAL or projection reconstruction MRI, the  $k$ -space is sampled with equally spaced radial lines, all of which traverse the center of  $k$ -space. It was the first trajectory to be used in an MRI experiment by Lauterbur in 1973 [1]. Today, radial MRI is particularly utilized in dynamic applications [2]–[5] that require a high temporal resolution while tolerating an increased artifact level in return. Undersampling in the azimuthal direction maintains the overall image structure and results in streaks instead of backfolding or discrete ghosting artifacts typically observed with Cartesian sampling [6]. Azimuthal undersampling may therefore speed up the image acquisition without sacrificing spatial resolution. Furthermore, in Cartesian imaging the contrast-relevant center of  $k$ -space is covered by only a part of the phase encoding steps. Hence, the time points

to be resolved are predefined by acquisition. In contrast, the fact that in radial imaging each profile incorporates data from the center of  $k$ -space potentiates the more frequent reconstruction of images in dynamic MRI. Sliding window reconstruction techniques have been presented to increase the image update rate [7] and to retrospectively choose between a limited number of spatial and temporal resolutions [8]. However, these methods do not provide full flexibility in depicting arbitrary time frames of arbitrary temporal resolution. The user always requires some *a priori* knowledge about the expected motion kinetics and the needed temporal and spatial resolutions, which often vary during scanning.

To overcome the loss in spatial resolution caused by undersampling, the high spatial frequencies can be replenished by data from other time points by  $k$ -space filtering. Initially, Song *et al.* [9] have proposed such a filter [termed  $k$ -space weighted image contrast (KWIC)] to reconstruct different contrasts from one multi-echo data set. Since then, others have adopted this approach for fast parameter mapping [10]–[12], in dynamic studies of the biodistribution of a contrast agent [13], [14] and for time-resolved contrast-enhanced three-dimensional (3-D) MR angiography [5]. For the usage of contrast-enhancing  $k$ -space filters, data are segmented and arranged in undersampled sweeps, as many as time points have to be resolved. To resolve one of these time points, the sweep representing the time point of interest is fully utilized, while omitting  $k$ -space center data of all other sweeps, such that they solely contribute to the less densely sampled high frequency periphery. Contrast-enhancing  $k$ -space filters increase the image update rate without sacrificing spatial resolution. However, it is not possible to depict time points other than those predetermined by the filter design e.g., to address periods of fast changing contrast or to further increase the temporal resolution by arbitrarily downsizing the data set.

All of these techniques make radial MRI an adjuvant sampling strategy in dynamic studies of contrast evolution or motion kinetics, taking advantage of the redundant sampling of the  $k$ -space center. However, all approaches presuppose the adjustment and coordination of a number of parameters before an experiment, involving extra time for the planning of a scan and requiring *a priori* knowledge about the expected motion or contrast kinetics.

This work investigates a novel sampling strategy for radial MRI that facilitates and supports the usage of radial MRI in dynamic or contrast studies. The method acquires profiles spaced by a constant azimuthal increment of  $111.25^\circ$ . This angle is related to the Golden Ratio and causes radial lines to be very evenly spaced with time [15], [16]. A similar pattern can be found in nature: leaves of plants often grow in this particular

Manuscript received February 23, 2006; revised September 13, 2006. Asterisk indicates corresponding author.

\*S. Winkelmann was with the Institute of Biomedical Engineering, University of Karlsruhe, Germany. She is now with Philips Research Europe, 22335 Hamburg, Germany (e-mail: etefanie.winkelmann@philips.com).

T. Schaeffter was with the Philips Research Europe, Hamburg, Germany. He is now with the Division of Imaging Sciences, King's College London, U.K. (e-mail: tobias.schaeffter@kcl.ac.uk).

T. Koehler and H. Eggers are with Philips Research Europe – Hamburg (e-mail: Thomas.Koehler@Philips.com, Holger.Eggers@Philips.com).

O. Doessel is with the Institute of Biomedical Engineering, University of Karlsruhe, Germany (e-mail: Olaf.Doessel@ibt.uni-karlsruhe.de).

Digital Object Identifier 10.1109/TMI.2006.885337

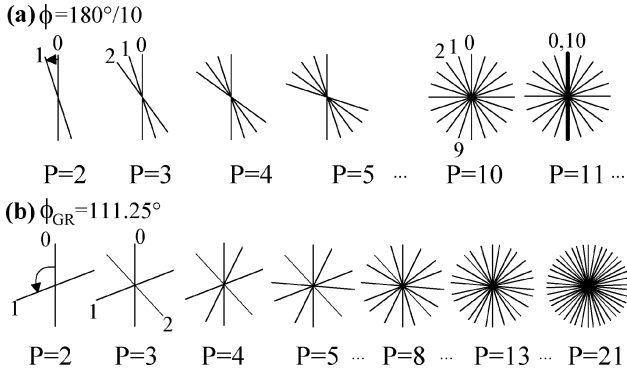


Fig. 1. (a) Profile order based on a fixed increment, which is only optimal for  $P = 10$ .  $P < 10$ : Profiles are not distributed over the entire radial space.  $P > 10$ : Profiles are sampled more than once. (b) Profile order based on the Golden Ratio. The angle increment of  $111.25^\circ$  is determined by dividing  $180^\circ$  according to the Golden Section. This guarantees an optimal profile distribution for any arbitrary number of profiles used in reconstruction, especially for  $P$  being a Fibonacci number.

order to ensure as little overlap as possible with previously grown leaves. The profile order is evaluated and compared with a uniform profile spacing in terms of SNR and artifacts. It was utilized in two applications: for dynamic cardiac imaging and multiple contrast reconstruction from one single inversion recovery shot of the brain by  $k$ -space filtering.

## II. METHODS AND MATERIALS

### A. Theory

1) *An Azimuthal Profile Spacing Based on the Golden Ratio:* In radial or projection reconstruction MRI, the  $k$ -space trajectory consists of  $P$  lines, also called views or profiles that all traverse the  $k$ -space center. Two temporally succeeding profiles are usually spaced by the constant angle increment  $\phi_{\text{uniform}} = 180^\circ/P$ . For a set of exactly  $P$  profiles, this provides the most uniform azimuthal data distribution [Fig. 1(a)]. However, to guarantee an optimal distribution of an arbitrary number of radial profiles, this work investigates an azimuthal spacing of  $\phi_{GR} = 180^\circ/\gamma$  for two succeeding profiles.  $\gamma = (\sqrt{5} + 1)/2 = 1.618$  is known as the Golden Ratio or Golden Section and solves the equation  $\gamma^2 = \gamma + 1$ . Note that the Golden Ratio is strongly related to Fibonacci numbers  $F(k) = \{1, 1, 2, 3, 5, \dots\}$  ( $F(k+2) = F(k+1) + F(k)$ ,  $k \geq 0$ ) as the ratio of adjacent Fibonacci numbers approximates  $\gamma$ . By choosing this fixed angle increment, the following features are achieved.

- Each profile added to a preceding set of acquired profiles divides one of the largest azimuthal gaps occurring in the golden section [Fig. 1(b)] [17].
- If the number of profiles  $P$  equals a Fibonacci number, only two different azimuthal gaps occur. The preceding two Fibonacci numbers determine their frequency of occurrence (example:  $P = 34 = F(8)$ ). There are only two azimuthal gaps that occur between neighbor profiles in  $k$ -space. The larger one,  $\Delta\phi_1$ , appears  $F(7) = 21$  times, the smaller one,  $\Delta\phi_2$ , appears  $F(6) = 13$  times. In case

of  $P$  not being a Fibonacci number, only three different azimuthal gaps occur (see Appendix ).

- As the sampling scheme is based upon a constant angle increment, a window that is temporally moving or “sliding” by  $n \cdot \text{TR}$  (repetition time) selects a constant sampling pattern that is rotated by a constant increment of  $\phi = n \cdot \phi_{GR}$ .

Points 1 and 2 imply an almost uniform sampling pattern, where undersampling artifacts are always distributed over the entire radial space. According to the above considerations, this profile spacing guarantees that samples are very evenly distributed in azimuthal direction for any arbitrary number  $P$  of succeeding profiles Fig. 1(b), and thus, it allows the *a posteriori* adjustment of the temporal resolution of selected time frames. Furthermore, stated in point 3, these time frames may be further positioned anywhere within the acquisition train without changing the contemplated sampling pattern.

2) *Sampling Pattern:* Suppose that the sampling interval  $\Delta k_{\text{readout}}$  in the readout direction permits the artifact-free reconstruction of  $M$  pixels (between  $-k_{\text{max}}$  and  $+k_{\text{max}}$ ) to depict the field of view  $\text{FOV} = 1/\Delta k_{\text{readout}}$ . Then, in a radial sampling pattern, the Nyquist criterion is satisfied if the distance or the azimuthal gap between samples in azimuthal direction  $\Delta\phi$  does not exceed the sample distance in readout (or radial) direction  $\Delta k_{\text{angular}} \leq \Delta k_{\text{readout}}$ . This corresponds to  $\Delta k_{\text{angular}} = \Delta\phi \Delta k_{\text{readout}} M/2 \leq \Delta k_{\text{readout}}$  or, respectively, it requires that the azimuthal gap  $\Delta\phi$  does not exceed the Nyquist limit  $\Delta\phi \leq 2/M = \Delta\phi_{\text{Nyquist}} = \pi/P_{\text{Uni,Nyquist}}$ . Thus, in a uniform profile spacing,  $P_{\text{Uni,Nyquist}} = M \cdot \pi/2$  radial profiles have to be acquired, in order to fulfill Nyquist in the outermost region of  $k$ -space [18]. In the case of the Golden Ratio based profile order, the size of the azimuthal gaps varies not only with  $P$  but also with the azimuthal direction. Hence, for the same number of profiles used, the compliance with  $\Delta\phi_{\text{Nyquist}}$  is generally not guaranteed, and thus, the Nyquist criterion is not fulfilled for all  $k$ -space regions. The largest occurring azimuthal gap (see the Appendix ) in a Golden Ratio based profile order is

$$\Delta\phi_{\text{max}}(P) = \begin{cases} g(1-g)^{i-1} \cdot 180^\circ & F(2i) \leq P < F(2i+1) \\ (1-g)^i \cdot 180^\circ & F(2i+1) \leq P < F(2i+2) \end{cases} \quad (1)$$

for  $i > 0$  and with the Fibonacci numbers  $F(k)$  and  $g = 1/\gamma = 0.618$  being the inverse Golden Ratio. Given that there are always only two (if  $P \in F$ ) or three (if  $P \notin F$ ) different azimuthal gaps (see Appendix ), if azimuthal undersampling needs to be avoided, the number of profiles  $P_{GR, \text{Nyquist}}$  should be chosen as the lower of the two Fibonacci numbers, such that it satisfies  $\Delta\phi_{\text{max}} \leq \Delta\phi_{\text{Nyquist}}$  in (1).

The weighting function  $W$ , being the inverse of the sample density  $D$ , affects the sampling efficiency, the SNR and the artifact level of a trajectory. According to [2], the local weighting function  $W$  can be approximated by the areal extent  $A(k_r, k_\phi)$ , underlying each pixel  $(k_r, k_\phi)$ . Assuming a constant sample spacing in readout direction of  $\Delta k_r = k_{r+1} - k_r = 1$ ,  $A(k_r) = 2\pi k_r$  describes the ring-shaped area incorporating all samples at a radial distance  $k_r$  from the  $k$ -space center. Then, the fraction  $A(k_r, k_\phi)$  of this ring occupied by a certain sample is given

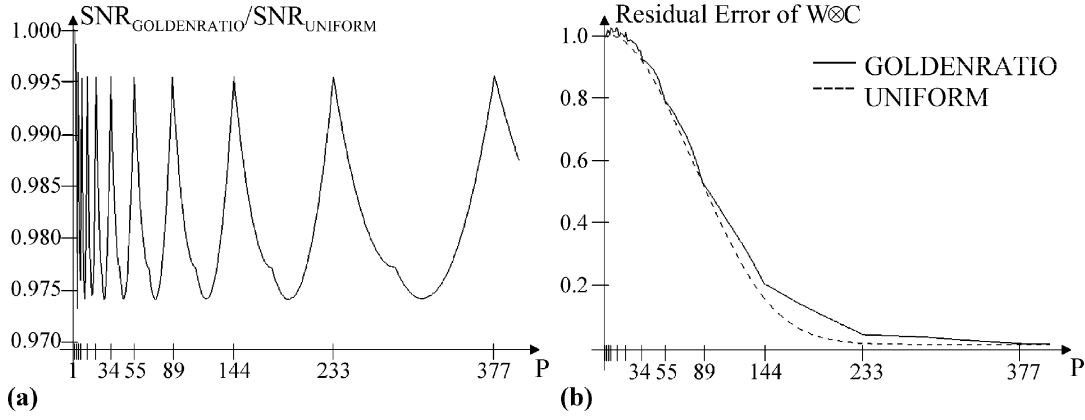


Fig. 2. (a) Ratio of the SNRs of a uniform profile order and a Golden Ratio based profile order. The ratio never falls below 0.973 and is optimal (maximum at 0.995) if  $P$  equals a Fibonacci number. (b) Residual error of the magnetization transfer function for a uniform and a Golden Ratio based profile order. The residual error function for the Golden Ratio based profile order decreases linearly between two adjacent Fibonacci numbers.

by weighting  $A(k_r)$  with its relative local azimuthal distance to the adjacent profiles, so that

$$D^{-1} = W = A(k_r, k_\phi) = \frac{\Delta\phi}{2\pi} A(k_r) = \Delta\phi \cdot k_r. \quad (2)$$

3) *SNR and Artifact Level*: In contrast to a uniform profile spacing, the sample density in the azimuthal direction is not homogeneous, which has an impact on the image SNR and the artifact level. The ratio of the SNRs  $\text{SNR}_{\text{GOLDENRATIO}}$  and  $\text{SNR}_{\text{UNIFORM}}$  equals the ratio of the sampling efficiencies [19]. The latter depend on the homogeneity of the sample distribution achieved by each acquisition scheme and thus the two-dimensional (2-D) integral over the respective weighting function  $W$ . Using (2), the ratio of the SNRs can be shown to be

$$\begin{aligned} \frac{\text{SNR}_{\text{GOLDENRATIO}}}{\text{SNR}_{\text{UNIFORM}}} &= \sqrt{\frac{\int \int W_{\text{UNIFORM}} k_r \cdot dk_r dk_\phi}{\int \int W_{\text{GOLDENRATIO}} k_r \cdot dk_r dk_\phi}} \\ &= \sqrt{\frac{\frac{\pi^2}{P}}{\sum_{i=0}^{P-1} (\Delta\phi_i)^2}} \end{aligned} \quad (3)$$

with  $\Delta\phi_i$  being the mean azimuthal distance of the profile  $i$  to its adjacent profiles. Fig. 2(a) depicts this ratio for different numbers of profiles according to (3). The ratio is optimal (maximum at 0.995) if  $P$  equals a Fibonacci number and never falls below 0.974, even if  $P \notin F$ . Again, this implies a high degree of homogeneity of the sample distribution in azimuthal direction for an arbitrary number  $P$  of profiles.

As previously mentioned, the weighting function has furthermore impact on the artifact level. According to [20], the optimal weighting function is determined, so that the convolution of the weighting function  $W$  and the gridding kernel  $C$ ,  $W \otimes C$ , referred to as modulation transfer function, is unity at every sampling coordinate ( $W \otimes C \equiv 1$ ). Therefore, the point spread function (PSF), the Fourier Transform of the modulation transfer function, is described by a sinc function. Azimuthal undersampling introduces “Nyquist holes” i.e., unmea-

sured regions in  $k$ -space and therefore deviations of the modulation transfer function from unity. The resulting error is reflected in the PSF by a broadening of the main lobe or by increased side lobe amplitudes. According to Parseval’s theorem, this affects the image with equal energy, perceivable as blurring and aliasing artifacts. Pipe *et al.* [21] give a worst-case measure for a mean residual error throughout  $k$ -space by integrating  $(1 - W \otimes C)^2$  and dividing by the area of integration  $A$

$$\varepsilon = \frac{1}{A} \int_0^\pi \int_{-k_{\max}}^{+k_{\max}} (1 - W \otimes C)^2 dk_r dk_\phi. \quad (4)$$

The graphic in Fig. 2(b) illustrates the mean residual errors according to (4) for both the uniform and the Golden Ratio based profile order for different numbers of profiles  $P$  and  $M = 208$ . The gridding kernel used is described later in this section. The residual error in case of the proposed sampling scheme decreases nearly linearly between two adjacent Fibonacci numbers  $F(k) \leq P \leq F(k+1)$  and is generally slightly larger than for a uniform sampling pattern. Given a uniform profile order, the residual error is 1.15% for  $P_{\text{Uni}, \text{Nyquist}} = M \cdot \pi/2 = 327$ , required to satisfy Nyquist for  $M = 208$ . In comparison, given a Golden Ratio based profile order and  $P_{\text{GR}, \text{Nyquist}} = 377$  profiles, which is the minimum to avoid azimuthal undersampling for  $M = 208$ , the residual error is comparably low at 1.3%.

## B. Reconstruction

Prior to gridding reconstruction data are corrected for incoherent phases at  $k = 0$ . In radial imaging, a miscentered  $k$ -space trajectory leads to serious image artifacts, as the MR signals from different readouts do not contribute coherently at the center of  $k$ -space. Some sources of such trajectory misplacements are system latencies and imperfections of the gradient waveforms induced by eddy currents. Rasche *et al.* [22] had proposed to compensate for trajectory misplacements by correcting for linear phases along the one-dimensional (1-D) projections and absolute phase differences at  $k = 0$ . To separate system and object induced phases, the linear or first-order phase of a projection has to be computed with respect to two adjacent projections

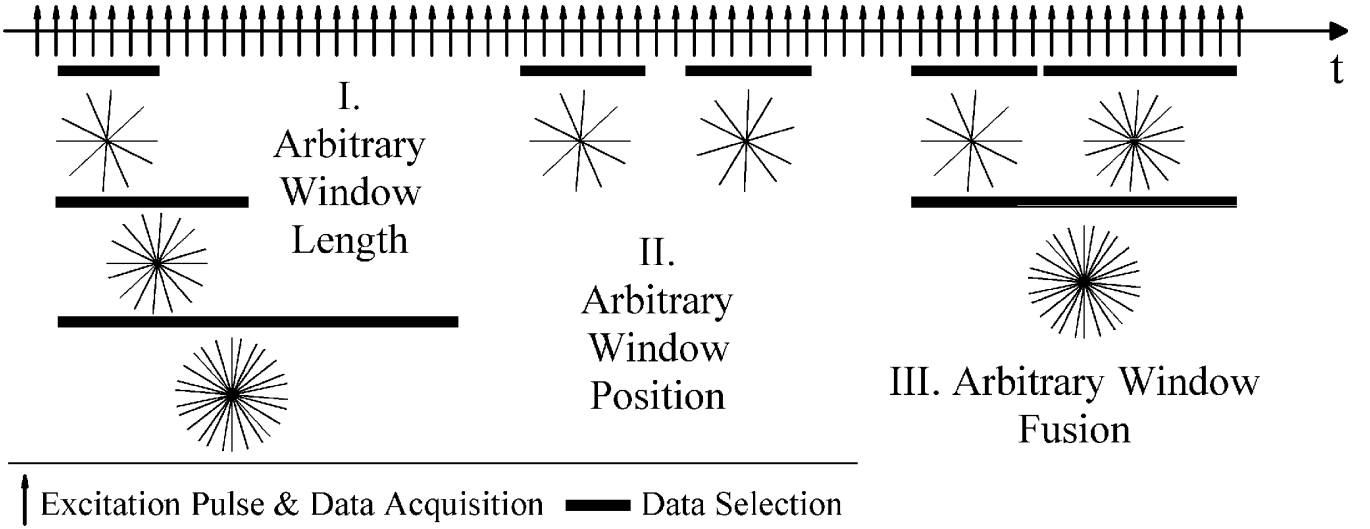


Fig. 3. The golden ratio profile order yields a high flexibility (I) in choosing an appropriate window length/temporal resolution, (II) in positioning the reconstruction window and (III) in combining adjacent time frames. This permits an extension of the sliding window reconstruction to variable window lengths and arbitrary window positioning.

from radial lines sampled in anti-parallel or near-antiparallel directions. In case of a Golden Ratio based profile order, the linear phase of one profile is computed with respect to the two nearest profiles that are approximately sampled in reversed direction. As two adjacent profiles are not necessarily sampled in near-antiparallel directions, the respective profile/neighbor combination setup was determined by an iterative search. For on-the-fly reconstruction, it has to be carried out only once before a dynamic experiment since the outcome of the search applies to all data sets of the same number of profiles. When images are reconstructed retrospectively from a dynamic acquisition train, the whole data set can be corrected at once before reconstruction windows are selected.

After the phase correction data are density corrected according to the considerations in (2). A Kaiser-Bessel-Window was used as the convolution kernel  $C$  to interpolate data unto a Cartesian grid prior to Fourier Transform. The width of the kernel was set to four Cartesian increments.

### C. Applications

1) *Advanced Sliding Window Reconstruction:* In a dynamic experiment, successive profiles are spaced by the angle increment of  $\phi_{GR} = 111.246^\circ$ . From this data set, images can be reconstructed with (I) arbitrary temporal resolution, (II) at arbitrary time points, and (III.) as a combination of an arbitrary choice of succeeding subsets, as illustrated in Fig. 3. Point (III.) shows the possibility of reconstructing highly undersampled data sets for motion analysis and to add motion corrected image data retrospectively to obtain a morphologic image with higher spatial resolution. The sampling pattern is constant for a constant sliding window length and is only rotated about its center (II). Independent from the window length, however, profiles are always distributed over the entire radial  $k$ -space (I). It is thus possible to adjust the temporal resolution of the imaging window a posteriori with respect to variations in motion or contrast dynamics from the same data.

2) *Multiple Contrast Reconstruction:* In radial MRI, each profile contains the image (contrast) information at the time point of its acquisition. Therefore, a contrast-enhancing  $k$ -space filter can be devised, which is used to reconstruct images of different contrasts from one single raw data set that was acquired while contrast was changing. The acquisition train experiences the signal or contrast evolution due to relaxation or recovery after a contrast inducing prepulse or the administration of a contrast agent. Using the entire data set would lead to a mixture of contrasts in the reconstructed image as all profiles, representing different time points, contribute to the  $k$ -space center, which dominates the overall image contrast. A contrast-enhancing  $k$ -space filter eliminates  $k$ -space center data of profiles that do not represent the time point of interest while maintaining their contribution to the sparsely sampled high-frequency  $k$ -space periphery. For example, a fat-saturation or inversion prepulse is followed by a train of profile acquisitions [Fig. 4(a)]. For the generation of an image, representing an arbitrary time point  $T_i = i \cdot TR$  after the prepulse, a set of profiles acquired before and after a profile  $i$  are selected, defining the reconstruction window. The time point  $T_i$  itself is resolved by applying a contrast-enhancing  $k$ -space filter to this selection, which eliminates  $k$ -space center data of profiles acquired before or after  $T_i$  [Fig. 4(b)]. The radius of elimination grows with the temporal distance of a profile to  $T_i$ . The profiles, contributing to each keyhole ring, represent a subset of succeeding profiles, for which the Golden Ratio profile spacing also guarantees an optimal distribution. Hence, the contrast evolution after the prepulse can be depicted with a flexible temporal resolution  $\Delta T_i$ , by reconstructing an arbitrary number of images at arbitrary time points.

The design of the filter is merely a matter of optimization with respect to the Nyquist criterion. Considering that the largest azimuthal gap occurring in a set of profiles does not change, until the number of profiles exceeds a Fibonacci number (see the Appendix) and in order to guarantee that the maximum azimuthal gap  $\Delta\phi_{Nyquist}(P)$  is never exceeded in any of the filter an-

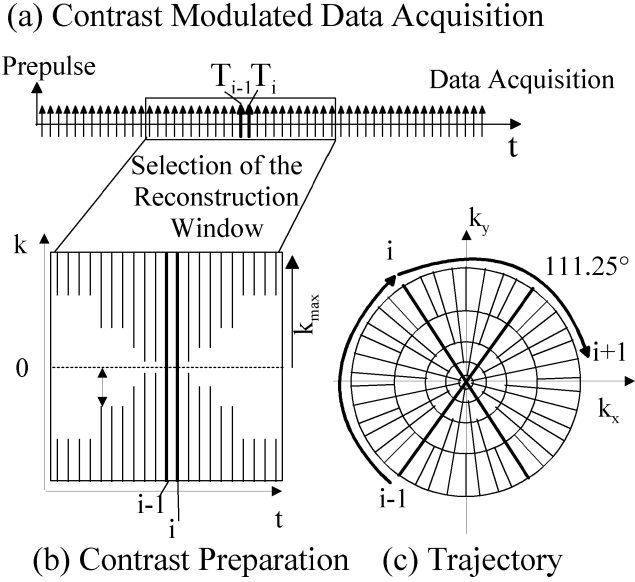


Fig. 4. (a) During acquisition the MR contrast is changing due to relaxation or signal recovery after a contrast modulating prepulse such as a fat saturation, inversion, or saturation pulse. Successive profiles are spaced by the angle increment of  $111.246^\circ$ . (b) An arbitrary time point  $T_i$  is selected by assigning the surrounding profile subset and deleting  $k$ -space center data of profiles acquired before  $T_{i-1}$  or after the selected time point  $T_i$ . The number of profiles per ring is given by Fibonacci numbers. (c) As the profile spacing provides an optimal profile distribution of an arbitrary subset of succeeding profiles, the distribution of the profiles in each filter ring is equally optimal.

nuli, the number of profiles in adjacent “filter rings” of the contrast-enhancing  $k$ -space filter is determined by Fibonacci-numbers, given by the inverse of (1). Thus, the innermost circle contains the two actual profiles acquired at  $T_i = i \cdot \text{TR}$  and  $T_{i-1} = (i-1) \cdot \text{TR}$ , the first ring contains 3 profiles followed by 5, 8, 13, 21, etc., profiles in the adjacent rings [Fig. 4(b)]. The resulting steps in the 1-D sampling density along the profile are smoothed by a polynomial function as described in [23]. Fig. 4(c) delineates the respective trajectory.

#### D. Experiments

All imaging was performed on a clinical whole-body scanner at 1.5T (Philips Achieva, The Netherlands) on healthy volunteers.

1) *Advanced Sliding Window Reconstruction Applied to Dynamic Cardiac Imaging*: Dynamic cardiac imaging of a healthy volunteer was performed using a steady state free precession (SSFP) sequence (FOV = 350 mm, Matrix  $128 \times 128$ , slice = 8 mm, flip angle =  $60^\circ$ , TR = 2.59 ms, 5 receive coils). An image was obtained by reconstructing all receive channels separately and summing up the squared results. For 10 s data were collected during free breathing. To depict the short systolic and the longer diastolic cardiac phase, the length of the sliding window was then retrospectively adjusted with respect to the position in the cardiac cycle. With respect to other gradient-echo methods, balanced SSFP sequences offer a superior SNR and contrast-to-noise ratio as well as an increased contrast between myocardium and blood. However, they are known to be very sensitive to rapidly varying eddy currents as produced by stepwise changing gradients [24]. To investigate the impact of

the large but constant azimuthal increment on the SNR and sequence related artifacts, the imaging experiment was repeated applying a uniform and linear profile order, a reconstruction window of 128 profiles and a sliding window factor of 2. This corresponds to the interleaved acquisition of two groups of 64 uniformly distributed profiles.

2) *Multiple Contrast Reconstruction for Fast  $T_1$ -Mapping of a Human Brain*: Images of multiple  $T_1$  contrasts of the head of a healthy volunteer were computed from a total of 1024 profiles following a nonselective inversion recovery prepulse (FOV = 250 mm, matrix =  $256 \times 256$ , slice thickness = 8 mm, flip angle =  $10^\circ$ , TR = 5.7 ms). The contrast-enhancing  $k$ -space filter was applied to data selections around different time points of interest  $T_i$ , sampling the steep part of relaxation more densely than the equilibrium. The size of these data sets was chosen such that Nyquist was satisfied in all  $k$ -space regions ( $P = 610$ ). The images were furthermore used for the computation of a parametric  $T_1$ -map of the brain using an exponential regression fit (Levenberg–Marquardt). Note that the continuous readout excitations accelerate the signal relaxation after the inversion pulse, so that the acquired data represent a shorter relaxation time  $T_1^*$ , which can be *a posteriori* converted into  $T_1$  by applying a correction factor that depends on the flip angle, and the repetition time described in [25].

### III. RESULTS

#### A. Sliding Window Reconstruction

To demonstrate the value of an arbitrarily sized window a series of images with varying temporal resolution was reconstructed (with  $P = 34, 55, 89, 144$ , and 233 resulting in temporal resolutions of 88, 142, 230, 373, and 603 ms, respectively). To depict the actual moments of cardiac contraction and relaxation, the reconstruction windows can be shifted in steps of one or more TR [Fig. 5(a)] and the length of the time frame can be retrospectively adapted according to the current cardiac motion. Fig. 5(c) shows the diastolic phase and Fig. 5(d) the systolic phase with the respective temporal resolutions. The image quality of the SSFP images was good [Fig. 5], with an SNR of 16 (systole, 55 profiles,  $\Delta T = 142$  ms) and 25 (diastole, 144 profiles,  $\Delta T = 373$  ms) and a low visual artifact level. Fig. 6 compares the images reconstructed from a uniform and a Golden Ratio based profile order. The ratio of the SNRs obtained in the blood with respect to the residual background signal was 0.954 and the image quality in terms of streaks and artifacts is visually comparable. Fig. 6(b) does not seem to suffer from image perturbation despite the SSFP sequence used and step-wise changing readout gradients.

#### B. Multiple Contrast Reconstruction

The flexibility in time point selection permits the reconstruction of arbitrary  $T_1$ -contrasts after one single inversion shot (Fig. 7), and thus, e.g., the depiction of the steep part of the relaxation curve with more images than the near-constant portion of the curve when the magnetization has reached its steady-state equilibrium value. The image series in Fig. 7 shows a maximum SNR of 24 and, visually, a low level of artifact. The first images of the series suffer from increased blurring, which can be

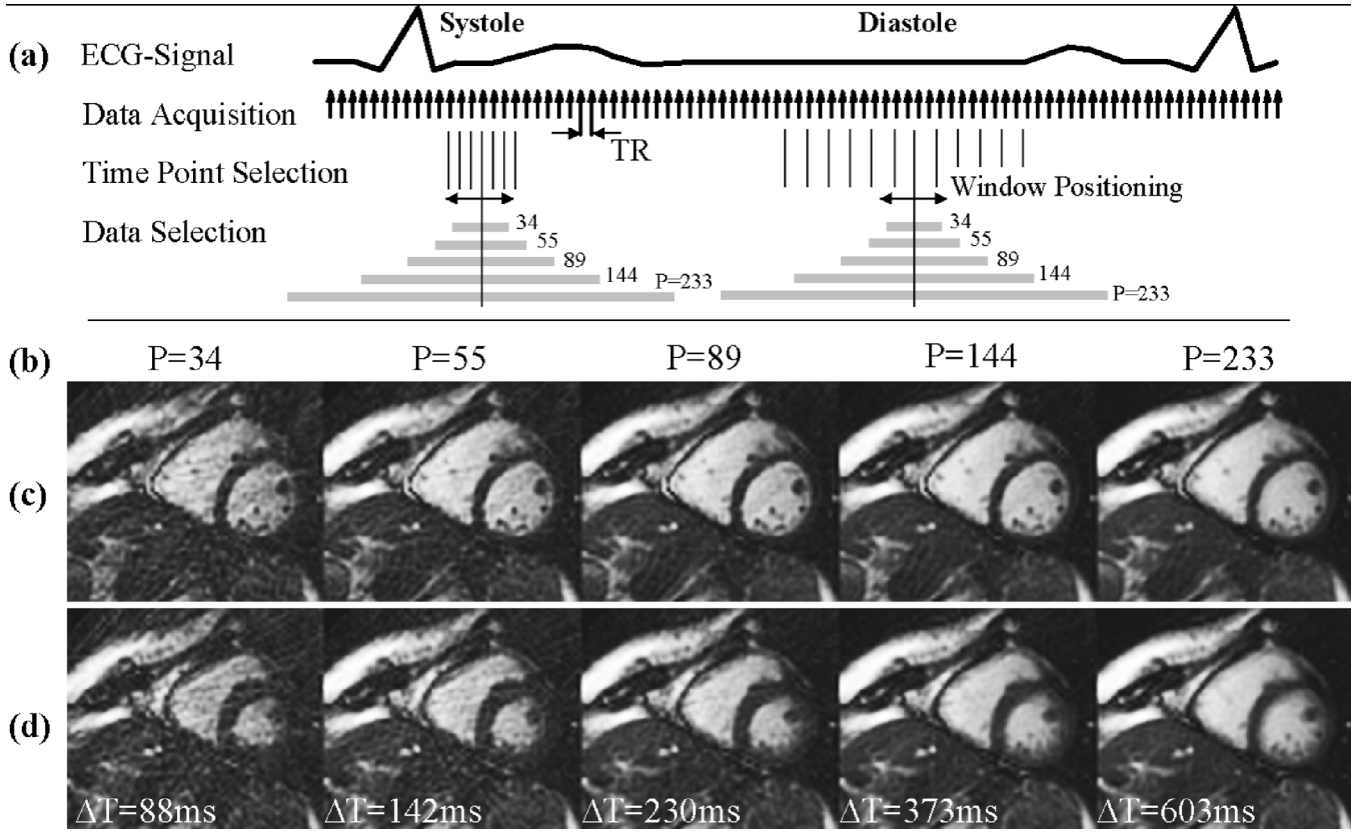


Fig. 5. Advanced sliding window reconstruction. (a) To depict the cardiac motion, images of different temporal resolution were reconstructed using data selections of 34, 55, 89, 144, and 233 profiles (respective to temporal resolutions of 88, 142, 230, 373, and 603 ms). To find the actual moments of cardiac contraction and relaxation, the reconstruction windows are shifted in steps of one or more TR. (b) Number of profiles per frame  $P$ . (c) Diastolic and (d) systolic cardiac phase reconstructed from the respective windows.

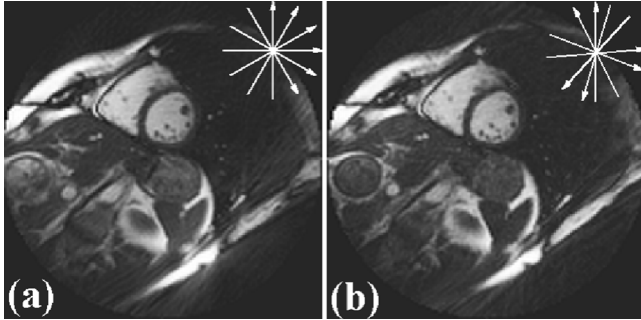


Fig. 6. Diastole reconstructed from 128 profiles ( $\Delta T = 330$  ms) using an SSFP sequence and (a) a uniform profile spacing with a sliding window factor of 2 and (b) a profile distribution based on the Golden Ratio. The images are of comparable quality.

explained by the low-pass filter effect of a contrast-enhancing  $k$ -space filter, in case that the signal intensity at low spatial frequencies is much higher than the overall average. Generally, one has to be aware of the fact that the mapping accuracy depends on the spatial frequency content or the size of the object under investigation and the filter radii applied to the  $k$ -space sample data [26]. Fig. 7(d) shows a  $T_1$ -map generated from the same single shot raw data set by selecting 20 time points temporally spaced by 300 ms ( $52 \cdot \text{TR}$ ). The  $T_1$  measurements yielded values of  $T_{1\text{gray}} = 987 \pm 72$  ms and  $T_{1\text{white}} = 649 \pm 87$  ms for gray and white matter, which matches well the values predicted by

literature that range from 920 ms to 1030 ms for gray matter and from 580 ms to 710 ms for white matter [27].

#### IV. DISCUSSION

The conventional uniform radial sampling scheme is restricted to a constant length of the acquisition window and requires a new scan for each desired temporal resolution. The proposed Golden Ratio based profile acquisition scheme provides a nearly uniform profile distribution for an arbitrary number of profiles. This involves some distinct advantages with respect to the conventional radial sampling.

First, it obviates any *a priori* planning and knowledge about the temporal resolution, the time point to reconstruct, the tolerable degree of undersampling, or the image update rate required. In cases where periods of different motion levels are indicated by sensors or by the images themselves, the number of profiles contributing to the reconstruction window can be adjusted retrospectively in order to always provide a flexible tradeoff between image quality and temporal resolution. For example, the length and position of the reconstruction window could be adapted according to the ECG signal indicating a systolic or diastolic phase, as was demonstrated in Fig. 5. Furthermore, sequentially acquired profiles are coarsely spread over the entire radial  $k$ -space spreading the effect of motion during acquisition. Additionally, the flexibility in data selection allows for the concurrent utilization of the same data for different purposes. Fig. 5

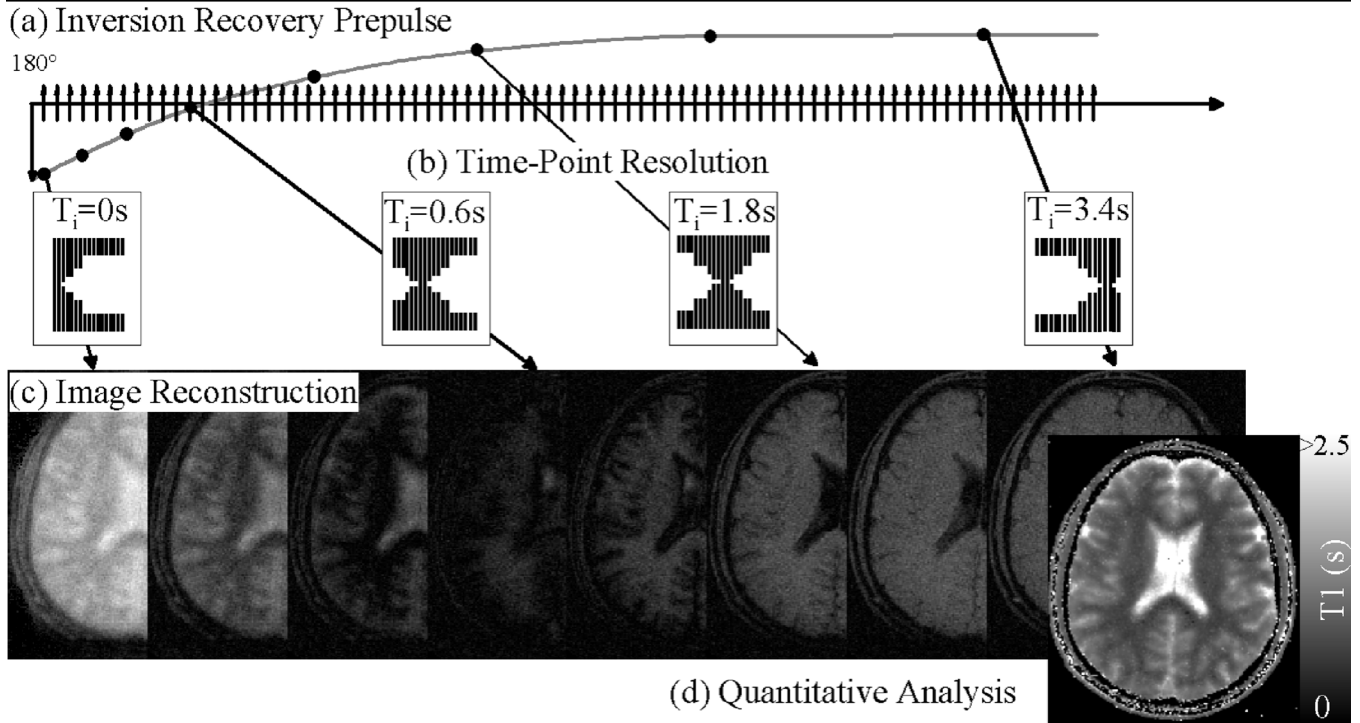


Fig. 7. (a) An inversion prepulse is followed by a train of low flip angle data acquisitions. (b) A contrast-enhancing  $k$ -space filter is applied to data selections that are large enough to satisfy Nyquist even in the  $k$ -space periphery to resolve different time points  $T_i$ . (c) Reconstruction of these preprocessed data sets yields images of different  $T_1$  contrasts. Figure shows 8 of 20 images that were reconstructed at certain time points of interest from one single inversion shot. (d) The image series can be consequently used for high-resolution single-shot  $T_1$ -mapping.

shows the possibility of an examination, in which motion is analyzed by coarsely sampled images and, using exactly the same data set, retrospectively adjusting the number, length, and position of the final reconstruction windows. For example, in the presence of arrhythmia the reconstruction window could be inherently adapted to the shorter or shifted period of low motion instead of rejecting the entire shot on account of some corrupted profiles. It was furthermore shown that the method can be combined with SSFP sequences, when eddy currents are less relevant and despite the significant but nevertheless constant jumps in  $k$ -space [24]. These come with a small reduction in SNR with respect to a uniform sampling pattern but image perturbations were not perceived (Fig. 6).

Second, equal flexibility is achieved for the use of contrast-enhancing  $k$ -space filters. The proposed order, when combined with a contrast-enhancing  $k$ -space filter, permits an arbitrary increase in the number of reconstructed images e.g., in order to address the high contrast variability at the beginning of a relaxation process. Furthermore, the large number of images produced from one single inversion shot has proven to be a sound basis for stable single-shot  $T_1$ -mapping [28]. Similar data processing strategies based on uniform sampling have been proposed for time-resolved contrast-enhanced imaging [5], [8]–[14]. These approaches need a presegmentation of the entire radial data set and an associated interleaving of the emerging subsets. When data segmentation is inherently given by the acquisition scheme (e.g., multiecho sequences), segmented filter approaches like the KWIC filter [9] or multitier method [26] are preferable. In contrast, the filter presented in this work addresses applications that face a continuous or

unknown contrast variability. For example, in dynamic contrast agent studies or after a contrast inducing prepulse the expected contrast kinetics or relaxation times may be hard to predict impeding a distinct segmentation precept. The inherent adaptability of time point resolution motivates automatic reconfiguration or self-calibration of the time point selection and reconstruction procedure without the need for additional scans. Regardless of the application, whether it is static radial imaging, dynamic sliding window reconstruction or time-resolved or contrast-resolved imaging, by using the proposed filter, the total time of the examination is reduced as one scan serves multiple purposes and the necessity of planning is alleviated.

For a number of applications, it could be interesting to extend the approach of the Golden Ratio based profile order from 2-D to 3-D, so that an arbitrarily undersampled 3-D data set is optimally distributed over the entire spheric space. In 3-D MRA of the extremities a flexible 3-D sliding window reconstruction potentially facilitates the time-resolved visualization of bolus inflow and in long 3-D scans, it would permit the computation and display of intermediate results for scan control purposes.

In summary, the choice of the angle increment determined by the Golden Ratio ensures that, given a profile set fully arbitrary in size, each succeeding profile divides one of the current largest azimuthal gaps. Thus, this method provides a nearly uniform profile distribution over the entire radial space for an arbitrary number of profiles. Overall, the acquisition becomes very insensitive to the temporal length of the reconstruction window. In conclusion, while a uniform profile distribution with a constant angle increment is optimal for a fixed and predetermined number of profiles, a profile distribution based on the

Golden Ratio proved to be an appropriate solution for an arbitrary number of profiles. Furthermore, the image quality, in terms of SNR and artifacts relative to the uniform sampling pattern, is comparable. Hence, the proposed profile acquisition scheme facilitates the use of radial imaging, making it a powerful sampling strategy especially in dynamic MRI applications that demand a high flexibility and adaptability of the reconstruction process to the temporal and spatial requirements.

#### APPENDIX

The appendix quantitatively investigates the azimuthal gaps  $\Delta\phi_1$ ,  $\Delta\phi_2$ , etc. (with  $\Delta\phi_1 \geq \Delta\phi_2 \geq \dots$ ) between adjacent profiles and their number of occurrence  $N\phi_1$ ,  $N\phi_2$ , etc., in a radial trajectory when sequentially measured profiles are spaced by a constant angle increment of  $\phi_{GR} = 111.246^\circ$ . This angle is obtained by dividing  $180^\circ$  according to the Golden Ratio. All angles are normalized to  $180^\circ$ .  $\phi \rightarrow \phi/180^\circ$ . All considerations are made on a semicircle, as profiles that radiate through the entire space produce a point symmetric pattern.

#### Fibonacci-Numbers

$$F(k) = \{1, 1, 2, 3, 5, 8, 13, 21, \dots\} \quad k \geq 0 \quad (A1)$$

$$F(k) = F(k-1) + F(k-2). \quad (A2)$$

#### Golden Ratio

$$\gamma = 1.618 \text{ and } g = \frac{1}{\gamma} = 0.618 \text{ with } g^2 = (1-g). \quad (A3)$$

When succeeding radial profiles are spaced by the angle increment  $\phi_{GR} = g$ , each additional profile divides the current largest azimuthal gap  $\Delta\phi_1$  by the golden section into the angles  $g \cdot \Delta\phi_1$  and  $(1-g) \cdot \Delta\phi_1$  [17].

*Hypothesis:* If  $P \in F(2i) = \{2, 5, 13, \dots\}$  ( $i > 0$ ), the azimuthal gaps to be expected are

$$\begin{aligned} \Delta\phi_1 &= g(1-g)^{i-1} & N\phi_1 &= F(2i-1) \\ \Delta\phi_2 &= (1-g)^i & N\phi_2 &= F(2i-2). \end{aligned} \quad (A4)$$

If  $P \in F(k=2i+1) = \{3, 8, 21, \dots\}$  ( $i > 0$ ), the azimuthal gaps to be expected are

$$\begin{aligned} \Delta\phi_1 &= (1-g)^i & N\phi_1 &= F(2i) \\ \Delta\phi_2 &= g(1-g)^i & N\phi_2 &= F(2i-1). \end{aligned} \quad (A5)$$

Note that  $N\phi_1$ ,  $N\phi_2$ , etc., are given for the semicircle.  $2 \cdot N\phi_1$ ,  $2 \cdot N\phi_2$ , etc., indicate the actual numbers of occurrence in a full circular space.

*Proof by Induction:*

$i = 1$ ,  $F(2i) = 2$ ,  $F(2i+1) = 3$ : Two profiles divide the semicircle in sections of  $g$  and  $(1-g)$ . A third profile divides

the larger section  $g$  into sections of  $g \cdot g = (1-g)$  [according to (A3)] and  $g(1-g)$ :

$$P = 2 = F(2) :$$

$$\Rightarrow \Delta\phi \in \{g, (1-g)\}$$

$$\Rightarrow \Delta\phi_1 = g = g(1-g)^{1-1} \geq \Delta\phi_2 = (1-g)^1$$

$$\Rightarrow N\phi_1 = 1 = F(2 \cdot 1 - 1), N\phi_2 = 1 = F(2 \cdot 1 - 2) \quad \checkmark$$

$$P = 3 = F(3) :$$

$$\Rightarrow \Delta\phi \in \{g \cdot g, g \cdot (1-g), (1-g)\} = \{(1-g), g(1-g)\}$$

$$\Rightarrow \Delta\phi_1 = (1-g)^1 \geq \Delta\phi_2 = g(1-g)^1$$

$$\Rightarrow N\phi_1 = 2 = F(2 \cdot 1), N\phi_2 = 1 = F(2 \cdot 1 - 1). \quad \checkmark$$

The Hypothesis holds for  $i = 1$ .

$n \rightarrow n+1$ : Assume, the Hypothesis in (A4), (A5) holds for  $i = n$ , then, for  $P = F(2n+1)$ ,  $\Delta\phi_1 = (1-g)^n$ ,  $\Delta\phi_2 = g(1-g)^n$ , with  $N\phi_1 = F(2n)$  and  $N\phi_2 = F(2n-1)$ . With each additional profile  $p$ , so that  $P = F(2n+1)+p$ , this angle is divided into the angles  $\Delta\phi_2 = g(1-g)^n$ ,  $\Delta\phi_3 = (1-g)^{n+1}$ . Hence,  $N\phi_1(p) = F(2n) - p$ ,  $N\phi_2(p) = F(2n-1) + p$ ,  $N\phi_3(p) = p$ .

$F(2n) \rightarrow F(2(n+1)) = F(2n+2)$ : Due to (A2) the total number of profiles reaches  $P = F(2n+2)$  after  $p = F(2n)$  profiles have been added to  $P = F(2n+1)$ . Thus, for  $i = n+1$  and  $P = F(2n+2)$

$$\Delta\phi_1|_{n+1} = \Delta\phi_2|_n = g(1-g)^n$$

$$\Delta\phi_2|_{n+1} = \Delta\phi_3|_n = (1-g)^{n+1} \quad \checkmark$$

$$N\phi_1(p)|_{i=n} = F(2n) - F(2n) = 0$$

$$N\phi_2(p)|_{i=n} = F(2n-1) + F(2n)$$

$$= F(2(n+1)-1) = N\phi_1|_{i=n+1}$$

$$N\phi_3(p)|_{i=n} = F(2n) = F(2(n+1)-2) = N\phi_2|_{i=n+1} \quad \checkmark$$

(The condition for  $P = F(2(n+1)+1) = F(2n+3)$  is analogously proofed by adding  $F(2n+1)$  profiles to  $P = F(2n+2)$ ).

*Conclusion:* The Hypothesis holds for all  $i > 1$ .

The proof also showed the following.

- For  $P \in F$ , there are only two different azimuthal gaps.
- For  $P \notin F$ , there are always three different azimuthal gaps.
- For  $P \notin F$ , the third azimuthal gap is obtained by dividing the current largest azimuthal gap  $\Delta\phi_1$  by the golden section into the existing gaps  $\Delta\phi_2 = g \cdot \Delta\phi_1$  and  $\Delta\phi_3 = (1-g) \cdot \Delta\phi_1$ .

#### ACKNOWLEDGMENT

The authors would like to thank D. Herzka from Philips Research, Briarcliff Manor, NY, for reviewing this manuscript and for contributing with some nice simulation movies.

#### REFERENCES

- [1] P. C. Lauterbur, "Image formation by induced local interactions: Examples employing nuclear magnetic resonance," *Nature*, vol. 242, pp. 190–191, 1973.



- [2] G. H. Glover and J. M. Pauly, "Projection reconstruction techniques for reduction of motion effects in MRI," *Magn. Reson. Med.*, vol. 28, pp. 275–289, 1992.
- [3] D. C. Peters, R. J. Lederman, A. J. Dick, V. K. Raman, M. A. Guttman, J. A. Derbyshire, and E. R. McVeigh, "Undersampled projection reconstruction for active catheter imaging with adaptable temporal resolution and catheter-only views," *Magn. Reson. Med.*, vol. 49, pp. 216–222, 2003.
- [4] D. C. Peters, F. R. Korosec, T. M. Grist, W. F. Block, J. E. Holden, K. K. Vigen, and C. A. Mistretta, "Undersampled projection reconstruction applied to MR angiography," *Magn. Reson. Med.*, vol. 43, pp. 91–101, 2000.
- [5] A. V. Barger, W. F. Block, Y. Toropov, T. M. Grist, and C. A. Mistretta, "Time-resolved contrast-enhanced imaging with isotropic resolution and broad coverage using an undersampled 3-D projection trajectory," *Magn. Reson. Med.*, vol. 48, pp. 297–305, 2002.
- [6] M. L. Lauzon and B. K. Rutt, "Effects of polar sampling in k-space," *Magn. Reson. Med.*, vol. 36, pp. 940–949, 1996.
- [7] V. Rasche, R. W. de Boer, D. Holz, and R. Proksa, "Continuous radial data acquisition for dynamic MRI," *Magn. Reson. Med.*, vol. 34, pp. 754–761, 1995.
- [8] H. K. Song and L. Dougherty, "Dynamic MRI with projection reconstruction and KWIC processing for simultaneous high spatial and temporal resolution," *Magn. Reson. Med.*, vol. 52, pp. 815–824, 2004.
- [9] —, "K-space weighted image contrast (KWIC) for contrast manipulation in projection reconstruction MRI," *Magn. Reson. Med.*, vol. 44, pp. 825–832, 2000.
- [10] M. I. Altbach, E. K. Outwater, T. P. Trouard, E. A. Krupinski, R. J. Theilmann, A. T. Stopeck, M. Kono, and A. F. Gmitro, "Radial fast spin-echo method for T2-weighted imaging and T2 mapping of the liver," *J. Magn. Reson. Imag.*, vol. 16, pp. 179–189, 2002.
- [11] M. A. Griswold, P. Schmitt, P. Speier, M. Nittka, V. Gulani, and P. M. Jakob, "Real-time undersampled radial IR-TrueFISP for fast quantitative T1, T2 & M0 mapping," in *Proc. ESMRMB 2004*, abstract 248.
- [12] A. F. Gmitro, M. Kono, R. J. Theilmann, M. I. Altbach, Z. Li, and T. P. Trouard, "Radial GRASE: Implementation and applications," *Magn. Reson. Med.*, vol. 53, pp. 1363–71, 2005.
- [13] H. K. Song, L. Dougherty, and M. D. Schnall, "Simultaneous acquisition of multiple resolution images for dynamic contrast enhanced imaging of the breast," *Magn. Reson. Med.*, vol. 46, pp. 503–509, 2001.
- [14] R. Lethmate, H. Ratiney, F. T. Wajer, Y. Cremillieux, D. v. Ormondt, and D. Graveron-Demilly, "Dynamic magnetic resonance imaging with radial scanning: A post-acquisition keyhole approach," *MAGMA*, vol. 16, no. 1, pp. 21–28, 2003.
- [15] T. Koehler, "A projection access scheme for iterative reconstruction based on the golden section," in *Proc. IEEE Nucl. Sci. Med. Imag. Conf.*, 2004, M10–200.
- [16] I. G. Kasantsev, S. Matej, and R. M. Lewitt, "Optimal ordering of projections using permutation matrices and angles between projection subspaces," *Electr. Notes Discrete Math.*, vol. 20, pp. 205–216, 2005.
- [17] M. Livio, *The Golden Ratio: The Story of Phi, The World's Most Astonishing Number*. New York: Broadway Books, 2002.
- [18] K. Scheffler and J. Hennig, "Reduced circular field-of-view imaging," *Magn. Reson. Med.*, vol. 40, pp. 474–480, 1998.
- [19] C. M. Tsai and D. G. Nishimura, "Reduced aliasing artifacts using variable-density k-space sampling trajectories," *Magn. Reson. Med.*, vol. 43, no. 3, pp. 452–458, 2000.
- [20] J. I. Jackson and C. H. Meyer, "Selection of a convolution function for fourier inversion using gridding," *IEEE Trans. Med. Imag.*, vol. 10, no. 3, pp. 473–478, Sep. 1991.
- [21] J. G. Pipe, "Reconstructing MR images from undersampled data: Data-weighting considerations," *Magn. Reson. Med.*, vol. 43, pp. 867–875, 2000.
- [22] V. Rasche, D. Holz, and R. Proksa, "MR fluoroscopy using projection reconstruction multi-gradient-echo (prMGE) MRI," *Magn. Reson. Med.*, vol. 42, no. 2, pp. 324–334, 1999.
- [23] S. Winkelman, T. Schaeffter, H. Eggers, and O. Doessel, "SNR enhancement in radial SSFP imaging using partial k-space averaging," *IEEE Trans. Med. Imag.*, vol. 24, no. 2, pp. 254–262, Feb. 2005.
- [24] O. Bieri, M. Markl, and K. Scheffler, "Analysis and compensation of eddy currents in balanced SSFP," *Magn. Reson. Med.*, vol. 54, pp. 129–137, 2005.
- [25] D. C. Look and D. R. Locker, "Time saving in measurement of NMR and EPR relaxation times," *Rev. Sci. Instrum.*, vol. 41, pp. 250–251, 1970.
- [26] M. I. Altbach, A. Bilgin, Z. Li, E. W. Clarkson, T. P. Trouard, and A. F. Gmitro, "Processing of radial fast spin-echo data for obtaining T2 estimates from a single k-space data set," *Magn. Reson. Med.*, vol. 54, pp. 549–559, 2005.
- [27] P. J. Jezzard, S. Duewell, and R. S. Balaban, "MR relaxation times in human brain: Measurement at 4 T," *Radiology*, vol. 199, pp. 773–779, 1996.
- [28] S. Winkelman, T. Schaeffter, H. Eggers, H. Dahnke, and O. Doessel, "Single shot T1-mapping using an optimized profile order based on the golden ratio," in *Proc. 13th ISMRM*, May 2005, p. 2406.